In Situ Scanning Electron Microscope Peeling To Quantify Surface Energy between Multiwalled Carbon Nanotubes and Graphene

Michael R. Roenbeck,[†] Xiaoding Wei,[§,†] Allison M. Beese,[§,⊥,†] Mohammad Naraghi,[†,¶] Al'ona Furmanchuk,[‡] Jeffrey T. Paci,[‡,#] George C. Schatz,[‡] and Horacio D. Espinosa[†,*]

[†]Department of Mechanical Engineering, and [‡]Department of Chemistry, Northwestern University, 2145 Sheridan Road, Evanston, Illinois 60208-3111, United States. [§]These authors contributed equally to this work. [⊥]Present address: Department of Materials Science and Engineering, Pennsylvania State University, University Park, Pennsylvania 16802. [¶]Present address: Department of Aerospace Engineering, Texas A&M University, 3141 TAMU, College Station, Texas 77843-3141. [#]Concurrent Address: Department of Chemistry, University of Victoria, British Columbia, V8W 3V6, Canada.

ABSTRACT Understanding atomic interactions between constituents is critical to the design of high-performance nanocomposites. Here, we report an experimental–computational approach to investigate the adhesion energy between as-produced arc discharge multiwalled carbon nanotubes (MWCNTs) and graphene. An *in situ* scanning electron microscope (SEM) experiment is used to peel MWCNTs from graphene grown on copper foils. The force during peeling is obtained by monitoring the deflection of a cantilever. Finite element and molecular mechanics simulations are performed to assist the data analysis and interpretation of the results. A finite element analysis of the experimental configuration is employed to confirm the applicability of Kendall's peeling model to obtain the adhesion energy. Molecular mechanics simulations are used to estimate the effective contact width at the MWCNT–graphene interface. The measured surface energy is $\gamma = 0.20 \pm 0.09\ \mathrm{J \cdot m^{-2}}$ or $\gamma = 0.36 \pm 0.16\ \mathrm{J \cdot m^{-2}}$, depending on the assumed conformation of the tube cross section during peeling. The scatter in the data is believed to result from an amorphous carbon coating on the MWCNTs, observed using transmission electron microscopy (TEM), and the surface roughness of graphene as characterized by atomic force microscopy (AFM).

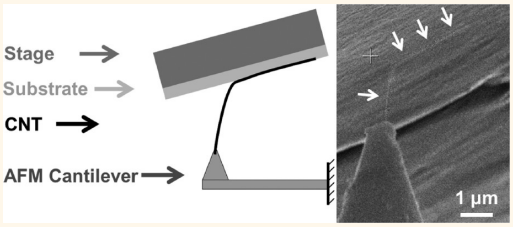

KEYWORDS: carbon nanotubes · graphene · *in situ* SEM testing · adhesion energy · molecular mechanics · chemical functionalization

Over the past several years, researchers have attempted to scale up the high strength-to-weight ratio of carbon nanotubes (CNTs) by incorporating CNTs in macroscopic yarns and composite materials. Researchers have developed a number of techniques to make macroscopic yarns, for instance, (i) dry spinning of CNT yarns by drawing and twisting from CNT arrays, aerogels, or mats[1−8] and (ii) wet spinning of CNT yarns by drawing and twisting from CNT sources embedded in chemical solutions.[9,10] Even though the procedures are different in technical details, all the yarns share CNTs as the smallest building blocks within the yarns. At the nanoscale, the load is carried by the tube–tube interactions through van der Waals forces between carbon atoms, noncovalent bonds between functional chemistries on the surfaces of CNTs, or covalent bonds through cross-linking between tubes. One major challenge researchers are facing is that although individual CNTs are strong and stable due to sp^2 bonding between carbon atoms, tube–tube interactions are relatively weak. This has resulted in the relatively inferior mechanical properties of CNT yarns compared to those of their constituents.[7,11−14] Therefore, researchers are investigating various approaches to increase the tube–tube interactions.[11] Several means of enhancing CNT–CNT interactions have been proposed, including inducing covalent cross-linking between individual CNTs and bundles of CNTs *via* high-energy radiation[15,16] and chemically derived surface functionalizations.[17−22] However, these treatments, aimed at increasing interaction between adjacent tubes, come at the expense of introducing structural defects in the CNTs themselves. Very few publications to-date report on experimental studies of

* Address correspondence to espinosa@northwestern.edu.

Received for review May 16, 2013 and accepted December 16, 2013.

Published online December 16, 2013
10.1021/nn402485n

the mechanical properties of pristine or functionalized surfaces at the tube level.[23−25] Consequently, there is a demand for developing an experimental technique that can characterize the tube interface properties at the tube−tube level. Here we propose an *in situ* experimental approach that can be used to investigate the effects of various chemical modifications on the material properties of tube surfaces.

Rather than having perfectly aligned CNTs, yarns consist of complex CNT networks, due to randomness and entanglement in the CNT sources. Some alignment is typically achieved during the spinning process. In the context of this study, yarns produced by twisting and stretching ribbons of freestanding mats of CNTs are of particular interest.[7,26] The smallest constituents in macroscopic yarns spun from such mats are CNTs, which are arranged into bundles typically exhibiting some degree of orientation. These bundles form a network leading to filament structures.[7,26,27] This complex structure results in various deformation and failure mechanisms acting at each length scale: from failure of the CNTs themselves, to peeling or shearing of the CNTs within bundles, to peeling or shearing from adjacent CNT bundles, where the network of bundles is subjected to macroscopic axial elongation. At the tube level, the interface failure between adjacent CNTs in a macroscopic yarn can be classified as either peeling, shearing, or mixed modes. Peeling resembles Mode I fracture, while shearing corresponds to Mode II fracture. If CNTs were perfectly aligned with one another along the axis of the fiber, shearing would be expected to be the predominant mode of failure. However, as perfect alignment of all of the CNTs within a yarn cannot be achieved, it is important to also characterize peeling. Developing an understanding of shear and peeling behavior between individual CNTs can provide mechanistic understanding of various functionalizations for improved CNT−CNT interactions, leading to higher-performance CNT-based yarns. Shearing *in situ* scanning electron microscopy (SEM) of CNTs was recently addressed by Espinosa and co-workers.[28] In this manuscript, we extend the work to peeling.

The peeling of CNTs from a substrate has been investigated through both simulations and experiments. Sasaki *et al*. conducted molecular mechanics simulations of single-walled carbon nanotubes (SWCNTs) peeling from graphitic surfaces, showing that sufficiently long SWCNTs adhered to graphite would transition from a line contact regime to a point contact regime before separating completely during peeling.[29,30] Strus *et al*. used atomic force microscopy (AFM) to peel CNTs from various substrates and compared their force-*vs*-displacement relations with results from an elastica model.[31,32] They reported interfacial energy as the integral under experimentally obtained force-*vs*-displacement curves and verified the conformational states predicted numerically by Sasaki *et al*. Buchoux *et al*. also used AFM, in this case to peel CVD-grown SWCNTs from graphite and mica substrates.[33] They calculated adhesion energy normalized per unit length of the CNTs through a force balance by assuming that changes in the profiles of small-diameter tubes were negligible such that cantilever deflection and debonding length could be considered equal. Ishikawa *et al*. performed *in situ* SEM nanoscale peeling tests of a multiwalled carbon nanotube (MWCNT) from graphite using a novel device they developed with force and displacement resolutions similar to those of AFM.[34,35] They reported adhesive energy as the integral under the experimentally measured force-*vs*-displacement curve, and verified that this energy was larger than the energy required for pushing and rolling MWCNTs on graphite, as reported previously in the literature.[36,37] Ke *et al*. investigated self-peeling of SWCNT bundles through *in situ* SEM experiments.[38] They applied classical peeling analysis to compute the energy release rate at the peeling point normalized by bundle bending stiffness, without measuring force. These studies did not provide a direct measurement of the surface energy in terms of energy per unit area, so it is difficult to compare the performance of each system in terms of normalized material properties.

To fill in this gap, we present an approach combining *in situ* SEM peeling experiments and theoretical computations. This study focuses on evaluating the surface energy of individual MWCNTs peeled from a graphene substrate. The direct visualization of the peeling process through *in situ* SEM testing, combined with force measurements, provides fundamental insights into the nanoscale interactions between these materials. When combined with an analytical model, finite element simulations, and atomistic calculations, the approach also enables the estimation of energy contributions within the framework of fracture mechanics. The method presented here is envisioned as a technique that can be used to evaluate the effect on nanoscale interactions between CNTs caused by chemical functionalizations, with the results presented here serving as baseline values for interactions between nonfunctionalized CNTs.

Experimental Methodology. In the peeling tests, as-produced MWCNTs were attached to, and subsequently peeled from, a substrate of graphene on copper (Figure 1) in order to experimentally evaluate the surface energy between the CNT and graphene. Within an SEM chamber, a tube was attached to the tip of an AFM cantilever of known stiffness that extended from a nanomanipulator. The tube was manipulated such that it lay on a graphene substrate mounted on an SEM stage. After a line contact was formed between the tube and the graphene, the stage was pulled away from the fixed cantilever to peel the tube from the graphene substrate. Images of the peeling process

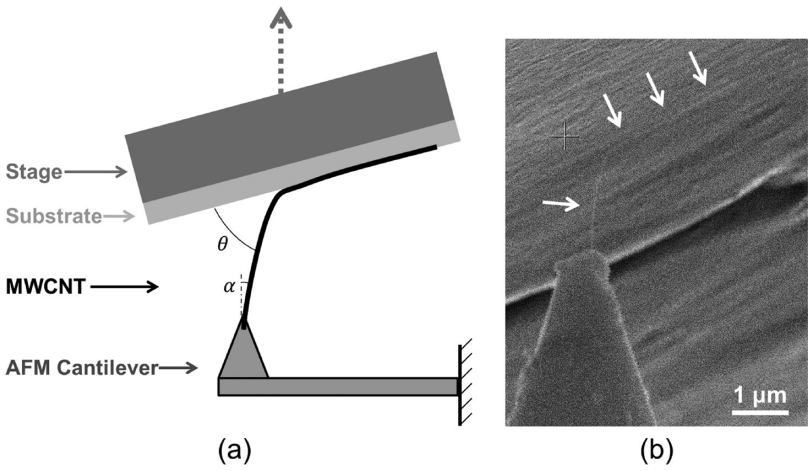

Figure 1. *In situ* **SEM peeling setup. (a) Testing schematic. A MWCNT is adhered to a graphene surface at an angle θ with an offset α, both of which can be characterized directly from SEM images. The stage is then slowly pulled away, causing the MWCNT to peel from the graphene substrate. (b) SEM image of a MWCNT carbon welded to a cantilever tip and in contact with a graphene surface. Arrows denote the path of the CNT, including the line contact beneath the three top arrows.**

were recorded to track both the profile of the tube and the deflection of the AFM cantilever. The vertical peeling forces were calculated by visually tracking the cantilever deflection and accounting for the offset angle, α (see Figure 1). After each test, the profile of the fully separated CNT was compared with its original shape to ensure the tube remained straight and did not change in length. For data analysis after the test, the peeling angle and cantilever deflection immediately preceding a peel were evaluated and used to calculate the surface energy of the CNT−graphene interface.

In theory, peeling two layers of graphene as opposed to peeling a MWCNT from graphene will benefit the surface energy calculation by simplifying the contact width determination. However, we chose the MWCNT−graphene system for experimental reasons. On the basis of our experience, manipulating graphene, a 2-D material, is much more difficult than manipulating a carbon nanotube, which is a 1-D material. In addition, there are several problems that could result from using a graphene layer instead of a carbon nanotube. For example, graphene tends to form tapered sections with uneven cross-sectional widths, as highlighted by Sen *et al.*[39] Variable contact width along the length of the graphene layer could not be assessed in SEM due to resolution limitations. An additional challenge could arise pertaining to manipulation: one would need to ensure that the two-dimensional graphene sheet adheres well to the AFM cantilever. Typical methods of adhesion, such as amorphous carbon deposition, may not work properly for welding homogeneously along the contact line for a 2-D material to provide a well-defined boundary condition. Furthermore, since this study is envisioned as a test bed for assessing the changes in surface energy associated with chemical functionalization, treatment of a monolayer of graphene may reduce the structural integrity of the layer. Such effects should not be as drastic for MWCNTs, where the inner shells should remain intact despite outer surface chemical functionalization. Therefore, MWCNTs are chosen in the current study.

The structures of 78 representative MWCNTs were examined using high-resolution transmission electron microscopy (HR-TEM) (Figure 2a and Figure 2b). The number of walls in each tube used in the experiments was estimated from the HR-TEM characterization of 20 tubes (among the 78 tubes investigated) with outer diameters similar to those measured in the *in situ* SEM experiments. From the TEM images, the outer diameter and number of walls in each tube were measured from line scans transverse to the main axis of the CNT. Linear interpolation of the number of walls as a function of tube outer diameter provided a statistical basis for estimating the number of walls within tubes tested in the SEM. While TEM images of this representative set showed that some tubes (Figure 2a) were relatively free of amorphous carbon coating, others (Figure 2b) were heavily coated. The potential effects of this coating on peeling behavior are described in the General Discussion section. Raman spectroscopy was also performed on the tubes to assess the defect density. The ratio of the D to G peaks (Figure 2c) was approximately 0.1, indicating that the defect density of the tubes was low. The diameters of individual tubes used in the *in situ* SEM tests were measured by calculating the full width at half-maximum (fwhm) of line scans perpendicular to the main axis of the CNT in the SEM images of each tube.

Graphene was chosen as the peeling substrate because it mimics the interaction surface from which CNTs would peel within dry-spun CNT yarns. A representative SEM image of a graphene surface (Figure 3a) shows copper grain boundaries (thick dark lines) as

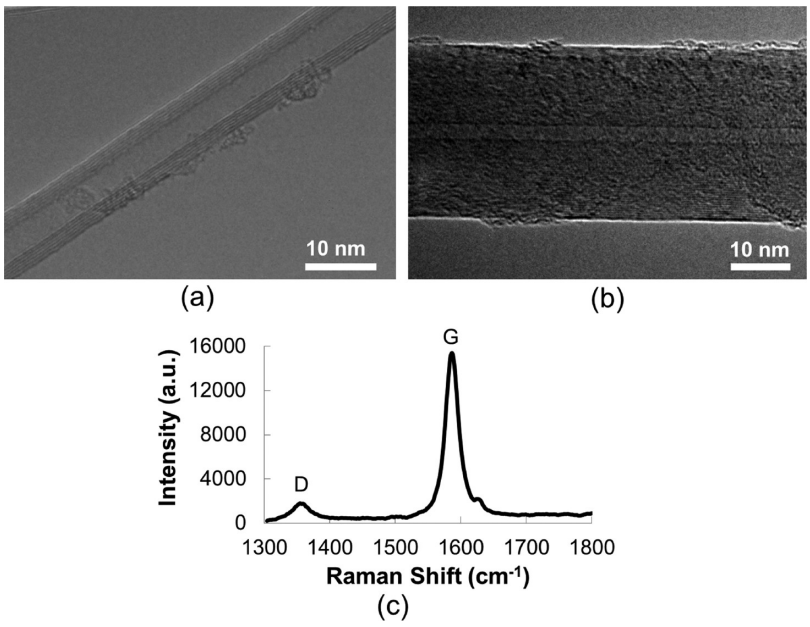

Figure 2. MWCNT sample characterization. (a, b) Sample HR-TEM images of as-produced arc-discharge MWCNTs. The tubes observed in the TEM were well-ordered and straight with variable amorphous carbon present on their outer surfaces. (c) Raman spectrum for MWCNTs. The ratio of the D peak to the G peak suggests that the defect density of the MWCNTs is low.

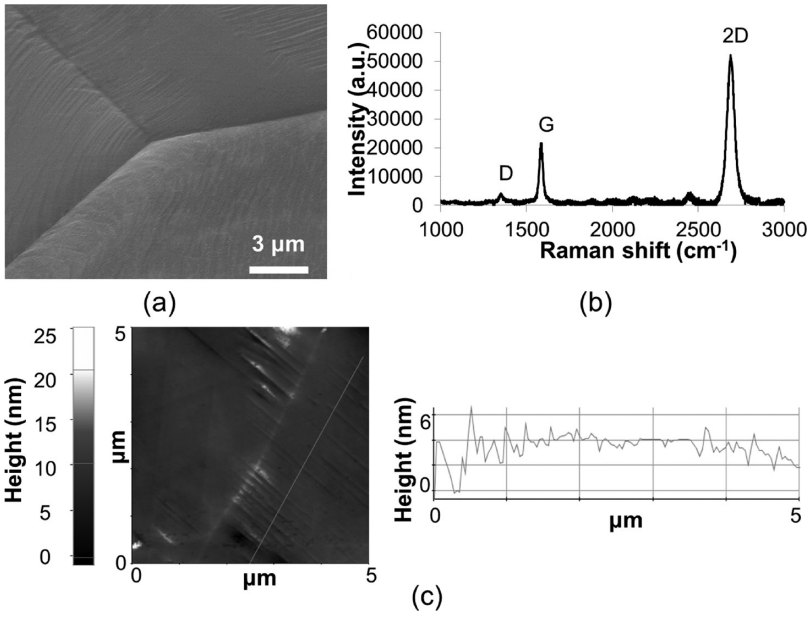

Figure 3. Graphene substrate characterization. (a) Representative SEM image of a graphene-on-copper surface showing three copper grains forming a junction. Wrinkles in various orientations are also apparent in the image. (b) Raman spectrum of graphene-on-copper surface. The presence of a G peak and a 2D peak are indicative of the presence of graphene on the surface. (c) Representative AFM image of a graphene-on-copper surface used to characterize wrinkles. Line scan over 5 μm indicates ripples are about 4 nm high and spaced ~200 nm apart.

well as the presence of small ripples (thin white lines). Copper grain boundaries were avoided during testing, as they were visible in the SEM. SEM images of the foil showed that copper grain boundaries were greater than 20 μm in any linear dimension, far exceeding the typical line contact region between the tube and the substrate (~3 μm). The topography of the graphene surface was characterized by atomic force microscopy (AFM) in noncontact mode, as shown in Figure 3c. Both atomically smooth and rippled regions were identified. The rippled regions had roughness values of approximately 4 nm in height with ~200 nm spacing between ripples. The effect of graphene roughness on the surface energy measurement will be described in the General Discussion section. Raman analysis of the graphene-on-copper foil exhibited the characteristic D, G,

and 2D peaks for graphene (Figure 3b). The ratio of the D to G peaks of 0.2 is indicative of a low defect density. Additionally, the ratio of the 2D to G peaks of ~2.4 confirmed that monolayer graphene was indeed present on the copper foil, where a ratio of *ca.* 2−4 is characteristic of monolayer graphene.[40−42]

As a means of validating the results of peeling from the graphene-on-copper foil, MWCNT peeling tests were also performed on freshly cleaved highly ordered pyrolytic graphite (HOPG) surfaces. HOPG has been used as a peeling substrate in previous CNT peeling studies, in part because topographical AFM scans have shown that the material is atomically flat.[31−35] While monolayer graphene-on-copper was the primary substrate used in the present study, results from peeling tests with HOPG further demonstrate the ability of the experimental method to acquire surface energies of unfunctionalized graphitic interfaces.

Kendall Analysis. MWCNT peeling studies were analyzed using the classical peeling formula developed by Kendall,[43] which assumes that an elastic film peels from a rigid substrate under a constant axial load, incrementally progressing the peel front without changing the shape of the film. The corresponding energy balance yields

$$F(1 - \cos(\theta)) = 2\gamma w - \frac{F^2}{2E\pi dt} \quad (1)$$

where F is the applied force, θ is the angle of the applied force with respect to the substrate (see Figure 1), γ is the interface surface energy, w is the contact width between the two surfaces, E is the elastic modulus of the CNT (E = 1 TPa[12,13,44]), d is the outer diameter of the CNT, and t is the single wall thickness (t = 0.34 nm, as we assume only the outer wall carries the tensile load). The term on the left-hand side of the equation corresponds to the external work of the cantilever acting on the CNT, while the first and second terms on the right-hand side of the equation denote changes in adhesion energy and changes in strain energy, respectively. In order to derive γ, w needs to be determined. Additional details describing the calculation of these parameters as well as the applicability of Kendall's formula to the peeling tests are included in subsequent sections.

Atomistic Methodology. Molecular mechanics simulations were used to determine the contact widths, w, by relaxing MWCNTs onto a single sheet of graphene using atomistic modeling techniques. Our model begins by considering a large defect-free graphene sheet that represents graphene on the surface of a polycrystalline copper foil. Recently published STM images of CVD grown graphene on polycrystalline copper foils indicate the presence of an intact graphene lattice.[45] It was also shown that the interaction of copper with graphene stimulates the partial dislocation of atoms in the surface layer of the copper substrate only. Therefore, we assume, similarly to the aforementioned experiments, that the carbon−carbon bonds in the graphene used here are not broken during peeling. Copper atoms are omitted in the present theoretical model since they are beyond the scope of this study. Instead, the copper−graphene interactions are modeled indirectly by assuming that the carbon atoms of the graphene layer are fixed in space after the structure is relaxed. As the analysis in the Atomistic Prediction of Contact Width section suggests, the presence of the copper instead of free space below the graphene is expected to change the surface energy by ~6%.

The large sizes of the experimental samples were addressed in the modeling by wrapping corresponding bonds and interactions in zigzag MWCNT-graphene structures across the longitudinal axial period of the sheet. Hydrogen atoms were added to graphene carbon atoms along the two other edges in order to eliminate edge effects in the nonperiodic directions. The length of MWCNTs in all simulations is 8 units (or 16 circumferential rings of carbon atoms). The procedure for choosing an appropriate axial length of the boundary box is described in the Methods section. In order to satisfy a minimum image criterion, the nonbonded cutoff was set to 12 Å.

All simulations were performed using the MM3 potential as implemented in the molecular mechanics package Tinker 6.0.[46] According to earlier studies,[47−49] the MM3 potential has been found satisfactory for describing CNT properties where C−C bond breaking does not occur. In particular, dispersion interactions are included so that nonbonded interactions common between proteins and CNTs are included. The carbon atoms were modeled as alkene (type 2) atoms. The potential energy of the structures in all simulations was minimized to an rms gradient of 0.0001 kcal/mol/Å. Zigzag CNTs with various numbers of walls were allowed to fully relax on the fixed graphene surface. Two protocols were used in relaxation calculations, designed to explore both collapsed and noncollapsed structures. In the first, the cylindrical shape of the CNT was deformed by applying displacements to selected atoms, in such a way as to try to induce collapse. At each step, the configuration of the tube was optimized subject to the displacement constraints. After the inner interwall distance reached 3.4 Å, all the constraints were released, and a full relaxation of the structure on the graphene surface was performed. In the second, full relaxations from the initially cylindrical starting structures were performed.

RESULTS AND DISCUSSION

Experimental Peeling Process. Forces exerted on the CNTs were obtained by digital image correlation of SEM images which tracked the deflection of the AFM cantilever throughout each peel test. The precise peel front propagation length was not required for Kendall's

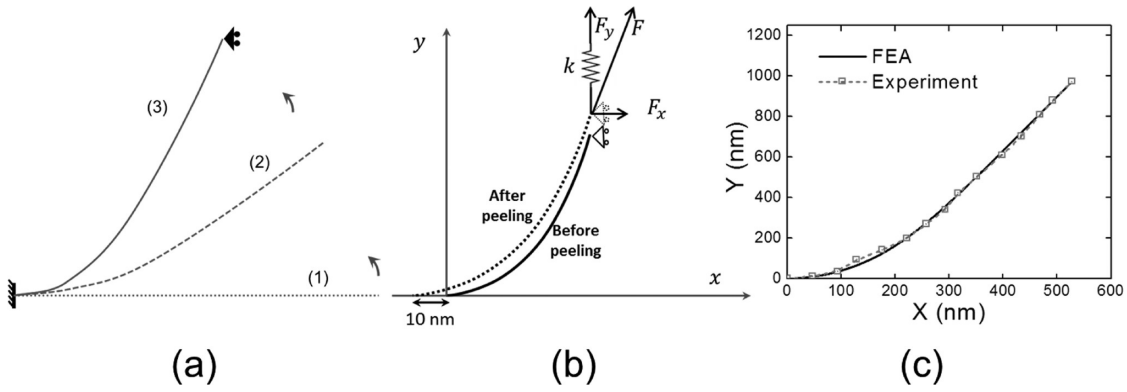

Figure 4. FEA simulations. (a) Schematic of the FEA simulation setup. An initially flat CNT with length matching that measured in the experiment is bent from configuration (1) to (2) to (3), with the left end held fixed. The right end in configuration (3) corresponds to the experimental measurement. A roller is added to the right end after configuration (3) to prevent the tube from translating horizontally during peeling. (b) Schematic of the FEA peeling model. The spring with constant *k* corresponds to the cantilever stiffness. The solid line represents the CNT configuration right before peeling, and the dashed line represents the CNT configuration after peeling 10 nm. (c) Comparison of the CNT shapes right before peeling obtained from the FEA simulation and experimental observation.

analysis, but an estimate of this helped determine whether or not the observed peel suffered from complications with the *in situ* experiment. In particular, peels with large displacements (~1 μm) and large fluctuations in force were not considered in the analysis, as they may have arisen from various experimental factors that could have led to excessively high forces and significant deviations from the Kendall analysis. Additional explanation of these factors is provided in the General Discussion section.

Finite Element Simulation Verification. While Kendall's formula is used in this study to calculate surface energy, the assumption of shape constancy during peeling does not apply in the employed experimental protocol, as the cantilever restricts the motion of the CNT. Hence, during a small but finite advancement of the peeling front, the shape of the tube changes slightly. The effect of this discrepancy between the experimental and analytical boundary conditions on adhesion energy is investigated using finite element analysis (FEA). In the FEA calculations, the tube was modeled as a 1-D beam with a cylindrical cross-section matching that estimated from experiments. Three-node quadratic beam elements were used to account for the tensile and bending deformations. As in Figure 4a, in the initial state (1), the CNT is straight and slack: no external loading is applied, and thus there is no strain energy in the system. At the left end of the tube, displacement and rotation were constrained, and at the right end, a spring element with a spring constant equivalent to that of the AFM cantilever used in the peeling experiments was connected to the tube. Note that during peeling, the AFM cantilever does not move horizontally but can move in the vertical direction. Hence, to obtain an initial shape consistent with the experiment, the spring element was progressively displaced until the position of the right end of the tube coincided with the position of the tube, just before peeling in an experiment (see Figure 4b). The FEA simulation predicted a tube profile that closely matched the experimental observation (see Figure 4c). At this configuration, the force applied at the right end of the tube, *F*, as well as the strain energy stored in the tube, $E_{initial}$, were obtained. To compute the energy release rate numerically, a virtual motion of the peeling front (10 nm in length) was assumed. After the system equilibrated, the strain energy of the tube after peeling, E_{final}, was obtained. Also, integrating the cantilever force *vs* cantilever displacement yielded the external work, W_{ext}, performed on the tube. Thus, according to Griffith's analysis,[50] the energy release rate, *G*, during peeling can be obtained numerically; namely,

$$G = W_{ext} - (E_{final} - E_{initial}) \quad (2)$$

To compare, Kendall's formula can also be applied to calculate the energy release rate. By inputting the cantilever force, *F*, and the peeling angle, θ, extracted from the simulation result right before peeling, the energy release rate given by Kendall's model is

$$G = F(1 - \cos(\theta)) + \frac{F^2}{2E\pi dt} \quad (3)$$

We performed FEM calculations on multiple peeling experiments (varying tube length and peeling angle) and consistently found only a 5% overestimation of the energy release rate by Kendall's model compared to Griffith's analysis. Thus, Kendall's analysis is used to compute the energy release rate from which γ is obtained.

Atomistic Prediction of Contact Width. Earlier studies[49,51,52] demonstrated that van der Waals interactions between CNTs and substrates can lead to deformation and even collapse of the tube, especially for nanotubes with large diameters. In addition, other observations suggest[53,54] that tube twisting may be used as a marker for detection of nanotube collapse.

Since only straight CNTs were observed in the current experiments, we assume that the MWCNTs are not collapsed before being put on the surface. However, depending on the diameter and number of walls, we expect some deformation on the graphene surface. Since it is difficult experimentally to determine the actual contact surface between the CNT and substrate, we have used atomistic modeling to describe the shapes of MWCNTs in these experiments. Such studies are well-known for SWCNTs and DWCNTs[49,55,56] of small diameters but not for MWCNTs.

The adhesion energy and, therefore, contact surface can be treated as a function of radial deformation of the MWCNT. To determine this contact surface, we need to define the operational range of van der Waals (vdWs) forces associated with contact between the nanotube and surface. A complete treatment of the vdWs forces should include Casimir effects in describing nanotube interactions.[57] However, we begin with considerations of the less-general Lennard-Jones potential given by

$$V = \varepsilon\left[\left(\frac{r_m}{r}\right)^{12} - 2\left(\frac{r_m}{r}\right)^{6}\right] \quad (4)$$

where ε is the well depth, and r_m is the separation distance at which the well has a minimum. For graphitic materials, it is known that $r_m \approx 3.4$ Å. At $r = r_m$, $V = -\varepsilon$. At $r = 2r_m$, $V = -0.03\ \varepsilon$. Thus, tube atoms at ~6.8 Å from the graphene sheet each contribute ~3% of the energy of an atom at the vdWs minimum. Not every atom within 6.8 Å of the graphene sheet contributes equally. Instead, those at the minimum separation make a full ε contribution and those at larger separations make a contribution scaled appropriately with distance. The energy differences between different locations in the vdWs registry are small (~50%) compared to the vdWs energy at the minimum.[58] Also, upon geometry optimization, atoms will take on geometries that tend to minimize their vdWs energies.

In the experiments, an atom in the MWCNT is interacting with all of the atoms in the graphene-on-copper. This implies that summing of the associated pairwise interactions is required. Steele has done such a summation for the (100) face of a simple cubic lattice, a result that depends on the position of the atom relative to the lattice.[59] It is also possible to replace the discrete set of atoms of the surface with a continuous distribution and to replace the sum with integration over the surface. The result is a 4,10 potential that describes the interaction between an atom and the surface as a function of separation.[59] It is given by

$$V_s(z) = 2\pi\varepsilon \sum_{k=1}^{\infty}\left\{\frac{2}{5}\left(\frac{1}{z^* + k}\right)^{10} - \left(\frac{1}{z^* + k}\right)^{4}\right\} \quad (5)$$

where k is an integer that indexes the planes, $z^* = z/(2^{-1/6}r_m)$, and z is the shortest distance between the atom and the surface. Steele showed that this provides a good approximation to the full-summation result, for separations between $\sim r = r_m$ and $r = 2r_m$ and beyond, for atoms that are the same size as those that comprise the surface (see Figure 2.3 of ref 59, solid dots). The expression goes as $1/r^3$ asymptotically (see also ref 60). The remaining sum is over planes, with the second plane contributing ~6% of the first. Similarly, replacing this final sum with an integral results in a 3,9 potential that does a poor job at approximating the full summation result for r less than approximately $4r_m$, but then provides the same result as the full sum out to asymptotically large distances, where it has $1/r^3$ behavior.[59]

Thus, one option is to use eq 5 to help in describing the interactions of the tube atoms within $\sim r_m$ to $2r_m$ of the surface; the experimental estimate of the energy of an atom at the vdWs minimum (0.26 J·m^{-2} ≡ 0.043 eV/atom) can be scaled using eq 5 for larger separations up to $2r_m$.[61−63] The curve predicted by eq 5 has a well depth that is approximately $^2/_3$ of that predicted by performing the full sum for an ideal-registry-type position (see Figure 2.3, curve "S", of ref 59). Including such a factor to scale down the well depth should be done to account for the inability of atoms to enter into ideal vdWs registry.

The geometry of the MWCNT−surface interaction in our molecular mechanics simulations is such that there were relatively few atoms that have $r_m < r < 6.8$ Å from the graphene surface (see Figure 5b), compared to the number of atoms with separations close to $r = r_m = 3.4$ Å. The $r_m < r < 6.8$ Å atoms are those present in the outer wall of the tube, near the edges of the flattened regions of the tube. The use of a cutoff distance larger than 6.8 Å would lead to a logical inconsistency because we are using a per atom energy based on graphite; thus, atoms in the second-to-outer wall of the CNT are part of the bulk-like graphite that make this energy approximation possible. To first approximation, the vdWs interaction "sees" into materials to a depth approximately equal to the separation (~3.4 Å in our case), suggesting our per atom approximation is reasonable.[64] There is evidence that as few as two to three layers of graphene or walls on a CNT are enough for the associated vdWs interactions to be close to those of bulk graphite.[65,66] A Lennard-Jones-based argument would suggest the same. TEM studies presented here suggest that the tubes used in experiments have greater than 10 walls, which is more than enough to justify this bulk approximation.

On the basis of the above discussion, the energy contribution of an atom in the outer wall of the tube can be estimated as

$$E_{at} = \frac{2}{3}\left[\frac{V_s(r_m + dz)}{V_s(r_m)}\right] 0.043\ \text{eV} \quad (6)$$

where $dz = z - r_m$, for atoms with $z \sim r_m$ to $z = 2r_m$. These atoms were those located near where restrictions

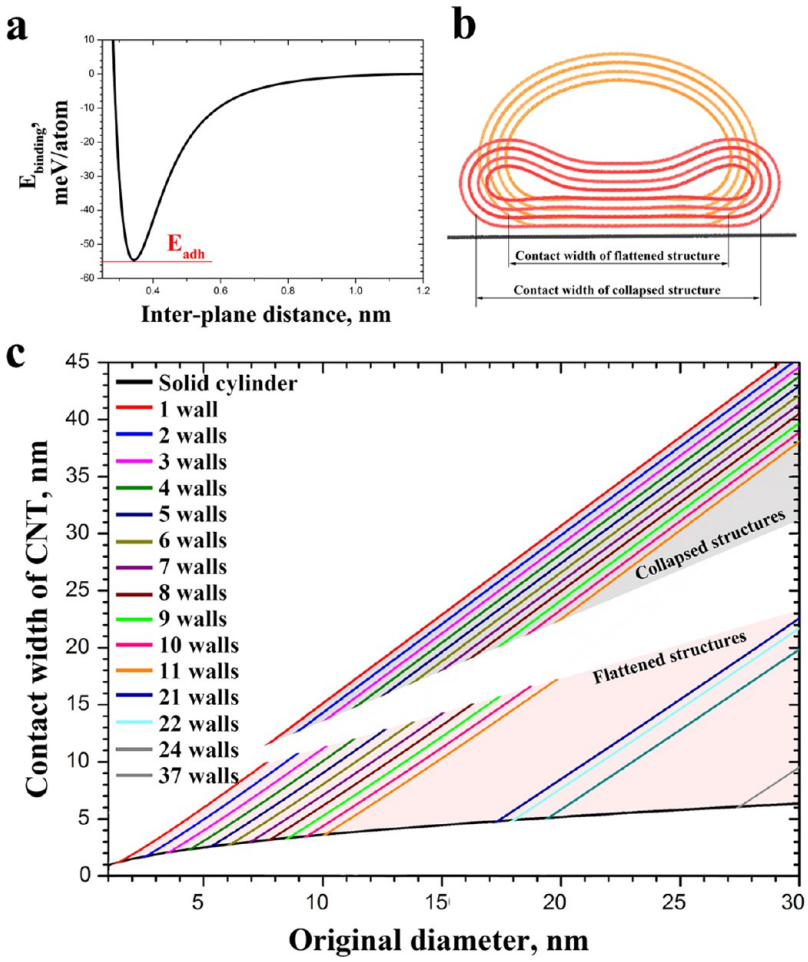

Figure 5. Molecular mechanics simulations of contact width. (a) The vdWs interaction energy per carbon atom based on interaction of graphene layers. (b) Flattened and fully collapsed structures that MWCNTs form due to interactions with graphene surfaces. (c) Contact width variation as a function of CNT diameter and number of walls. The region of fully collapsed structures is highlighted in gray, while the region of flattened structures is highlighted in pink. Each line corresponds to a certain number of walls.

due to the curvature of the tube confine them to this z range. Only $k = 0$ was used in the calculations of V_s, an approximation that should result in errors much less than the ~6% referenced above, due to cancellation of errors.

To show the effect of defining the contact width using a separation of ≤6.8 Å, we have performed two types of calculations using the MM3 MWCNT/graphene model. In the first, after relaxing the tubes on the graphene surface, the atoms located in the outer wall in a plane perpendicular to the longitudinal direction of the tube were identified for each segment of the tube. Then their positions were fitted to a polynomial function. The function values at ≤6.8 Å tube−graphene separation were used to determine the contact width. The values were averaged over all segments along the tube. In the second, we explicitly accounted for the fact that carbon atoms from the flat and curved segments of a CNT contribute differently to the adhesion energy. Initially, the van der Waals interaction energy per atom was calculated as a function of interlayer distance between two graphene sheets (see Figure 5a). Then, the integral of the binding energy over all atoms of a CNT was calculated based on eq 6. Comparison of the CNT−over−graphene binding energy with the one for graphene−over−graphene was then used to define the contact width. Both calculations resulted in contact width estimates that are effectively the same.

The degree of radial deformation of the CNTs is a function of the number of walls and the outer diameter. In the limit of large wall number and small outer diameter, no deformation occurs. In that case, the contact width can be calculated using an equation for a cylinder interacting with a stiff substrate:

$$w_{\text{cylinder}} = D\sqrt{1 - \left(1 - \frac{6.8}{D}\right)^2} \qquad (7)$$

where D and w_{cylinder} (black lines in Figure 5c, and Supporting Information, Figure S3, and Figure S7) are the diameter and contact width of a rigid cylinder,

respectively. Radial deformations become increasingly large with increasing diameter of the outer wall (pink region in Figure 5c). At some point the structures become flexible enough to collapse (gray region in Figure 5c). We determined from simulations that the point at which fully collapsed tubes are energetically stable is defined by the diameter of the inner wall. At an inner wall diameter of approximately 31 Å, contact between opposing tube sides is no longer sufficiently stabilized by van der Waals forces to prevent the tube from returning to a more cylindrical shape, regardless of how collapsed the initial tube geometry guess is. Therefore, the following equation was developed and used to determine the borderline below which full collapse is impossible:

$$D_{out} = D_{inner} + 2(\text{Inter})(N - 1) \quad (8)$$

where D_{out} is the outer diameter of the tube, D_{inner} = 31 Å, Inter = 3.4 Å is the interwall distance, and N is the number of walls. The tubes will be nearly cylindrical in cross section for $D < D_{out}$, for a given N. The four points adjacent to the solid cylinder line in Supporting Information, Figure S3 correspond to examples of such tubes.

For $D > D_{out}$, collapse is possible. For these diameters, the following equation was used for the collapsed width estimates (see the Methods section for parametrization details):

$$w_{collapsed} = 3.699 + 1.556D - 8.175N \quad (9)$$

where D is in Å. For each collapsed structure, a corresponding noncollapsed structure might also exist. Contact widths for such "flattened" structures can be obtained by applying corrections to eq 9 using:

$$w_{flattened} = w_{collapsed} - N\left(-0.00438 + \frac{0.41164}{N}\right)[(1 - H)D + H(A + B\exp(-D/C))] \quad (10)$$

where

$$H = \frac{1}{1 + \exp\left(\frac{-2(D - 8N)}{N}\right)} \quad (11)$$

$$A = 24.85 + 13.26N \quad (12)$$

$$B = -29.76 - 13.78N \quad (13)$$

$$C = 14.10 + 9.23N \quad (14)$$

Details of the development of these expressions can be found in the Methods section.

The stability of flattened *versus* collapsed configurations is determined by the balance between the force necessary to bend a graphitic sheet of a particular thickness, and the stabilization from van der Waals forces in the central collapsed region of the tube. If the central collapsed region is too small, the van der Waals forces do not provide enough stabilization, and the structure springs back to a flattened shape. Both flattened and collapsed structures may be stable, in which case there is an energy barrier associated with transforming geometry from one structure to another. At some D for a given N, flattened and collapsed structures are approximately energetically equal. We derived the following equation to describe the line separating the D and N values for which flattened *versus* collapsed structures are most stable:

$$20.196N + 215.954 = \pi D_{inner} \quad (15)$$

Supporting Information, Figure S4 is a cartoon illustrating the behavior captured by eqs 8 and 15. At even larger D values for a given N, only collapsed structures are stable (see Supporting Information, Figure S4d).

By summing pairwise vdWs interactions, the energy associated with a pair of planes can be calculated. It is given by[60]

$$W = \frac{-A}{12\pi D_p^2} \quad (16)$$

where A is a Hamaker coefficient and D_p is the distance between planes. The coefficient A is described by

$$A = \pi^2 C \rho_1 \rho_2 \quad (17)$$

where ρ_1 and ρ_2 are the numbers of atoms per unit volume, and C is the coefficient in the associated atom−atom pair potential, $W_p = -C/r^6$. Inclusion of Casimir effects (i.e., the full dielectric response of the material) does not change the form given by eq 17, but changes the expression for A.[60,64] Thus, the pairwise and full vdWs expressions for W have the same form.

For metals (including semimetals) in or near contact ($D_p \leq 20$ Å) in vacuum, $A \approx 4 \times 10^{-19}$ J,[60,64] so W = 0.092 J·m^{-2}. Two surfaces are created, so this gives a surface energy of 0.046 J·m^{-2}. However, as explained in ref 60, it is necessary to use a cutoff distance that is substantially less than the interatomic distance required to use eq 17 to calculate surface energies, as it is necessary to consider the atomic structure of surfaces when they are in contact. Using $\gamma = A/[24\pi(0.165\text{ nm})^2]$ as suggested in this reference gives γ = 0.2 J·m^{-2}, which is within experimental error of the average of the experimental values in previous reports (0.26 J·m^{-2}).[61−63]

It is also useful to consider estimating the energy contribution from the rounded areas where the tube flattening ceases, by using the Derjaguin approximation.[64] The approximation involves considering the surface of a material as a combination of piece-wise units that are parallel to the opposing surface, allowing for the use of eq 17 for each piece, and then summing. However, for the regions in question, the radius of curvature is not large compared to the separation between such

TABLE 1. Experimental Measurements and Calculated Surface Energy Values For Graphene-on-Copper and HOPG Substrates

substrate	tube no.	test no.	peel angle, θ [deg]	force, F [nN]	outer diameter [nm]	number of walls	adhesion energy, G (nJ·m^{-1})	collapsed contact width, w [nm]	flattened contact width, w [nm]	collapsed surface energy, γ [J·m^{-2}]	flattened surface energy, γ [J·m^{-2}]
graphene	1	1	66	14	30	37	8.3 ± 1.9	15.8	8.6	0.26 ± 0.08	0.48 ± 0.19
graphene	1	2	58	15	30	37	7.1 ± 1.8	15.8	8.6	0.22 ± 0.07	0.41 ± 0.17
graphene	1	2	56	13	30	37	5.6 ± 1.3	15.8	8.6	0.18 ± 0.05	0.33 ± 0.13
graphene	2	1	66	9	20	22	5.5 ± 1.1	13.5	7.7	0.20 ± 0.06	0.36 ± 0.14
graphene	3	1	68	2	19	21	1.2 ± 0.7	13.3	7.6	0.05 ± 0.03	0.08 ± 0.06
graphene	3	1	61	16	19	21	8.0 ± 1.5	13.3	7.6	0.30 ± 0.08	0.53 ± 0.20
HOPG	4	1	69	12	21	24	7.6 ± 1.2	13.8	7.7	0.27 ± 0.08	0.49 ± 0.19
HOPG	5	1	49	10	21	24	3.5 ± 0.6	13.8	7.7	0.13 ± 0.04	0.23 ± 0.09

regions and the graphene surface, so the approximation would not be very good.

Experimental Surface Energy. Experimental results for eight *in situ* SEM peeling tests are reported in Table 1. The tubes employed in the experiment had diameters in the range of 19−30 nm. Surface energy was calculated for each test using eq 1. The results listed for Tube 1 are from two subsequent tests with the same tube. SEM images of Tube 1 before and after the first test showed it maintains its straight profile before and after peeling. The results listed for tubes 2 and 3 are from single tests performed on each tube. In the case of tube 3, two peels were measured from the same test, but the tube was not disconnected between the peels.

To provide a thorough interpretation of the experimental results, we measure energy values in multiple forms (Table 1). First, we report adhesion energy per unit length, which makes no assumptions about the contact width at the interface. The average adhesion energy is 6.0 nJ·m^{-1} with a standard deviation of 2.6 nJ·m^{-1}. However, as noted previously, surface energy may be a more widely applicable metric to remove tube size dependency. Therefore, we report two columns of calculated surface energy values, which vary depending on the assumed conformation of the tube during peeling. If the tube is taken to be fully collapsed, the average surface energy is 0.20 J·m^{-2} with a standard deviation of 0.09 J·m^{-2}. If, instead, the tube is taken to be flattened, the average surface energy is 0.36 J·m^{-2} with a standard deviation of 0.16 J·m^{-2}. The largest scatter is found in the surface energy extracted from tube 3. This could be because this tube had the smallest diameter among those tested. As such, it is possible that tube 3 was affected more than the other tubes by factors discussed in the manuscript (contact conditions, surface inhomogeneities, contact width determination, *etc.*), resulting in larger variations in the measurement.

In addition, the results of two peels from an HOPG substrate, with applied loads and peeling angles similar to those reported with the graphene-on-copper substrate, are included in Table 1. The measurements fall within the range of values obtained with the graphene-on-copper substrate. Our simulations suggest that the lowest energy tubes in all tests were flattened; however, we also present surface energies for collapsed tubes, as experimental conditions may favor this metastable configuration (see Figure 5c). The variation among the results could stem from multiple sources, which merit a detailed discussion.

GENERAL DISCUSSION

First, it is worth noting how these experimental results compare to other results reported previously in the literature for related materials. In addition to studies with carbon nanotubes, direct comparison with the surface energy of bulk graphite is also appropriate based on the analysis described earlier.[65,66] There is some variation in the literature regarding accepted values for the experimental and theoretical surface energy of graphite, ranging from 0.035 J·m^{-2} to 0.875 J·m^{-2}.[61−63,67−73] Some experimental studies with graphite[67,74] report values of 0.19 and 0.33 J·m^{-2}. The results of the *in situ* SEM peeling tests reported here are in good agreement with the recent experimental surface energy studies of these carbon materials. The experimental scatter falls within the range of other previously reported experimental values for graphite.

There are several sources of experimental uncertainty and variability that may have contributed to the variation in calculated surface energies and deviations from the average experimental value of γ = 0.26 J·m^{-2} reported earlier.[61−63] For example, while MWCNTs developed through arc discharge only contain carbonaceous materials, amorphous carbon is present on the outermost layers of the tubes (e.g., see Figure 2), either directly from fabrication or due to induced amorphous carbon deposition by the electron beam in the SEM chamber. As this amorphous carbon lacks the well-ordered sp^2 bonding structure of carbon nanotubes and graphene surfaces, it may introduce additional interactions beyond what would be expected for idealized peeling between atomically smooth graphitic surfaces.[56]

Another source of scatter in the measured surface energy might be the roughness of the graphene surface. As shown in Figure 3, because of the different

thermal expansion properties of the copper foil and graphene membrane, the substrate exhibits some wavy regions after processing.[41,75−77] The rippled graphene will inherently affect the contact area at the interface. While limitations in SEM resolution prevent highly precise *in situ* characterization of peeling surfaces, deviations in surface roughness may also contribute to the measured surface energy.

The presence of molecules such as water in the SEM chamber may also affect the surface energy measured in this study. While *in situ* SEM tests were conducted in stable vacuum ($\sim 10^{-5}$ Torr), and tests were not performed until the tubes and graphene were in the vacuum for at least 2 h, molecules such as water may remain on both the carbon nanotube and graphene surfaces. When the surfaces come into contact, molecules on each surface may interact with one another and introduce additional interaction energy contributions. However, even if it were possible to conduct these tests in higher vacuum, this would present other challenges. For example, the time required for cutting the tubes during sample preparation would increase,[78] resulting in additional exposure of the CNT to the electron beam. The combinations of voltage and current conditions used during peeling and tube cutting in this study (see the Methods section), as well as the equilibration pressure conditions, reflect attempts to establish a compromise among the factors that must be considered in *in situ* SEM experiments.

Another experimental aspect to be discussed is the fact that the first tube was peeled multiple times. It could be argued that structural deformations at the atomic level may have formed after repeated peeling. Limitations in SEM resolution prevent investigations at this scale. However, the tube maintained a straight profile before and after testing, and the surface energy of the tube−graphene interface is consistent among the peeling tests. These observations suggest that any atomic-scale deformations did not significantly affect the surface energy values in this case. Nevertheless, the ideal study incorporating this method would only perform one peel test per tube to avoid this issue in the future.

Ultimately, this novel method enables direct visualization of peeling forces and displacements and provides substantial insights into MWCNT peeling behavior through direct integration of experiments and simulations. Although the primary substrate of interest in the current study is graphene-on-copper, the results from peels performed on HOPG are in good agreement with the former, and the values obtained with both methods compare favorably with the theoretical surface energy of graphite. These results with two distinct substrates further support the claim that this method is capable of experimentally ascertaining adhesion energies and surface energies. In addition, the consistency between each set of experimental results and the theoretical graphite surface energy suggests that both monolayer graphene and HOPG can be used as baseline substrates for evaluating the changes in surface energy associated with chemical functionalization.

CONCLUDING REMARKS

Here we report a new method for quantifying the surface energy of bare CNT−graphene interfaces through *in situ* SEM peeling experiments, which is combined with molecular mechanics and FEA simulations. Novel features of the method include direct visualization of the peeling and the estimation of contact width through detailed atomistic simulation, which allows the calculation of surface energy using fracture mechanics concepts. Average values of 0.20 ± 0.09 J·m^{-2} and 0.36 ± 0.16 J·m^{-2} for the surface energy of bare CNT−graphene surfaces were measured, depending on the assumptions made for the tube conformation during peeling. Both estimates of the surface energy agree with the average experimental value of 0.26 J·m^{-2} within the stated uncertainties. Potential reasons for variation including amorphous carbon interactions, molecules such as water on the graphitic surfaces, and substrate surface roughness are discussed.

The combination of experimental and computational studies in this work provides a foundation for understanding the interactions that occur between materials at the nanometer length scale. By investigating the behavior of these nanoscale building blocks, we aim to provide direction for enhancing surface interactions, for example, tube−tube, within larger-scale carbon-based yarns, and composites.

In addition to experimentally measuring the surface energy of bare tubes and graphene, this approach is also envisioned as a means of quantifying the changes in surface energy associated with chemical functionalization. Chemical cross-linking between nanoscale constituents could lead to the development of strong, lightweight yarns derived from CNTs, graphene, and other carbon materials that would be appealing for many potential applications, including next-generation textiles and artificial muscles.[1] The method presented here may serve as a test bed for a variety of chemistries in nanoscale peeling, providing a foundation for improving the mechanical performance of carbon-based materials from the bottom up.

METHODS

Materials. As-produced arc-discharge multiwalled carbon nanotubes (nTec) are used in this study because of their well-ordered structure, high-purity carbon content, and excellent mechanical properties as compared to tubes grown by chemical vapor deposition.[12] Geometries of representative MWCNTs are measured using high resolution TEM (JEOL 2100F). The primary substrate in

the peeling test is a mostly monolayer CVD-grown graphene on copper foil (Graphene Supermarket) analyzed using AFM (XE-120, Park Systems Corp.) and Raman spectroscopy (HR800, Horiba Jobin Yvon). Freshly cleaved HOPG (SPI) was also used as an additional graphitic substrate for validation.

Experimental Methods. The tests described here are carried out in an FEI NovaNano 600 SEM. Before testing, the SEM chamber is cleaned with oxygen plasma for at least 1 h to minimize sample contamination. MWCNTs are brushed onto a cut copper TEM grid and placed in the chamber together with a vertically oriented strip of graphene on copper. High-resolution pictures of selected MWCNTs are taken such that their diameters can be estimated by averaging, over multiple cross-sectional line scans, and calculating the full width at half-maximum of the average of the scans. For a given tube, an AFM cantilever (MikroMasch) of known stiffness is brought into contact with a dangling MWCNT using a nanomanipulator (Klocke). When the CNT is pulled taut, as determined from tube straightening, the CNT is cut with the electron beam at low voltage (5 kV) and high current (1.8 nA) based on established CNT cutting protocols.[78] All other manipulation of the samples takes place under high voltage (30 kV) and low current (~0.1 nA) in order to reduce amorphous carbon deposition and potential damage to the specimens.[78] After cutting, the MWCNT is welded to the surface of the AFM cantilever with electron beam-induced deposition of amorphous carbon at high magnification (~300 000×) for approximately 5 min. The length and orientation of the tube are recorded from images after this deposition to serve as a reference for checking whether any observable deformation of the tubes occurs after testing. The graphene surface is inspected to identify a flat location for placement of the CNT such that it will not interact with any visible imperfections. The graphene surface is rotated (approximately 30 degrees with respect to the cantilever arm) in order to promote peeling at low angles, reducing the likelihood of inducing structural changes in CNTs due to sharp bends and kinks.[79] In a given test, the force, F, is measured by digital image correlation of cantilever displacement including correction for cantilever drift. The offset angle, α, is measured directly from digital images in the frame before peeling.

Uncertainty Analysis. The analysis is based on uncertainties in the terms of the classical peeling formula developed by Kendall, eq 1. Experimental results indicated that the second term on the right-hand side of the equation, associated with strain energy, is much smaller than the other two terms in all tests. Consequently, uncertainty in strain energy is neglected for the purposes of this analysis.

The force F applied to the CNT during testing is measured as

$$F = \frac{k\delta}{\cos(\alpha)} \tag{18}$$

where k is the AFM cantilever stiffness, δ is the cantilever deflection, and α is the offset angle of the tube. The cantilever stiffness is given by

$$k = \frac{E_c w_c {t_c}^3}{4{L_c}^3} \tag{19}$$

where E_c, w_c, t_c, and L_c are the elastic modulus, width, thickness, and length of the cantilever, respectively. E_c is taken to be 169 GPa based on the established value for silicon in the ⟨110⟩ directions, in accordance with AFM cantilever manufacturing conditions.[80]

By rearranging eq 1 for surface energy γ and substituting eqs 18 and 19, the experimental uncertainty can be estimated by the square root of the sum of squared errors (see, e.g., ref 81) as

$$\frac{\Delta\gamma}{\gamma} = \left(\left(\frac{\Delta w}{w}\right)^2 + \left(\frac{\Delta\delta}{\delta}\right)^2 + \left(\frac{\Delta w_c}{w_c}\right)^2 + \left(3\frac{\Delta t_c}{t_c}\right)^2 + \left(3\frac{\Delta L_c}{L_c}\right)^2 + \left(\cot\left(\frac{\theta}{2}\right)\Delta\theta\right)^2 + (\tan(\alpha)\Delta\alpha)^2\right)^{1/2} \tag{20}$$

Among these components of uncertainty, the largest factor in any test is either uncertainty in contact width, w, or displacement, δ. To estimate uncertainty in adhesion energy, G, the same formula is used excluding the term for contact width.

The uncertainty in contact width arises from two features: the uncertainty in the number of walls of each MWCNT used for peeling, and the uncertainty in the measured outer diameter of each MWCNT. First, the outer diameters and numbers of walls of 20 arc discharge MWCNTs were measured using HR-TEM, which provide a statistical measure of the number of walls for a given tube diameter. Figure S1 (in the Supporting Information) shows the number of walls corresponding to each of the 20 tubes as measured from HR-TEM images. A linear best-fit interpolation is applied to estimate the number of walls corresponding to tubes of different diameters. For this sample of data points, the standard error of the estimate, s, is calculated to be ~2.7 from the variation between the linear fit and the experimental points. The parameter s is then rounded up to an integer number of walls, $s' = 3$, to provide a conservative estimate of this standard error over all diameters. An envelope (shaded region) is then defined to account for the tubes within $\pm 1s'$, as shown in Supporting Information, Figure S1.

Second, the outer diameter of each MWCNT used in testing is measured directly from SEM images. The outer diameter is measured by calculating the full width at half-maximum of brightness profiles corresponding to line scans across the longitudinal axis of the tube. Uncertainty in diameter associated with using this procedure is also incorporated into the total uncertainty in contact width. An uncertainty of $\pm$1.5 nm (1/2 pixel) is assigned to tubes 2 and 3, while an uncertainty of $\pm$2.9 nm (1 pixel) is assigned to tube 1 due to lower image quality.

The diameter and number of walls are then incorporated directly into the contact width formula derived from molecular mechanics simulations. For uncertainty considerations, two extremes are evaluated for each tube: the maximum diameter with the fewest number of walls, corresponding to a maximum contact width for a given tube, and the minimum diameter with the largest number of walls, corresponding to the minimum contact width for a given tube. The largest difference associated with these two extremes is taken as Δw.

Variation in displacement, δ, is taken as the difference between deflections measured by digital image correlation tracking two separate regions of the cantilever during each test, which should provide equivalent displacements. In the event of an exact match between the two measured deflections, an error of $\pm$1 pixel is assigned to reflect limitations in resolution of the digital image correlation software. Three independent experiments were conducted in which an AFM cantilever (extending from a nanomanipulator) and a TEM grid attached to the SEM stage were placed within the same viewing window and observed for several minutes (i.e., much longer than any individual peeling test). The results of these experiments indicated that AFM cantilever drift was linear with respect to time, while drift in stage position over time was negligible. Having established a basis for characterizing the cantilever drift as linear, the effect of drift on total displacement was determined and incorporated on a test-by-test basis, not by assuming a global rate of drift over all tests. Consequently, cantilever drift is accounted for by incorporating a linear estimate of drift contribution to displacement when reporting δ values in this study.

Variations in cantilever width w_c and cantilever thickness t_c are taken as the standard deviation of nine measurements of each of these values from SEM images. Uncertainty in cantilever length L_c is taken to be the same as the uncertainty in thickness associated with each cantilever. Deviations in θ and α are taken to be $\pm$2.5 degrees based on standard deviations of angles measured in a representative SEM image of a MWCNT. All variations in angle are assumed to be planar, as changes in out-of-plane orientation cannot be measured due to limitations in SEM depth of focus.

Typical experimental uncertainty values in surface energy associated with the assumptions presented here and incorporated into eq 20 were approximately 30% assuming the collapsed configuration and 40% assuming the flattened configuration. For adhesion energy, experimental uncertainty was approximately 20%.

Boundary Box Size Optimization Protocol for Atomistic Simulations. The graphene layer and zigzag (383,0) SWCNT were generated with VMD.[82] The (383,0) SWCNT was chosen to match the tube

diameter to experiments. Hydrogen atoms were added to the two graphene edges that are nonperiodic. Each structure was aligned in such a way that the periodic direction is always aligned with the *x*-axis of the simulation cell. The box *y*- and *z*-dimensions were set equal to 800 Å. The cell length along the periodic boundary was varied between 32 Å and 32.6 Å. For each such length the MWCNT (or graphene) structure was allowed to move until the total potential energy reached its minimum value. Final values were plotted as a function of the cell length (see Supporting Information, Figure S2).

The cell length associated with the energy minimum was assigned as the optimum longitudinal boundary. We assumed that the interaction of graphene with the copper foil prevents dramatic structural changes in graphene while it interacts with the CNT. Therefore, the optimum longitudinal cell length in this study was chosen equal to that from the graphene curve (32.2991 Å).

Parameterization for Fully Collapsed Structures. To obtain the collapsed configurations, the tubes were deformed by applying displacements to selected atoms, which tended to induce collapse. At each step, the configurations of the tubes were optimized for the given displacement constraints. After the inner interwall distance reached 3.4 Å, all constraints were released, and full relaxations of the structures on the graphene surface were performed. For tubes with small diameters or large numbers of walls, the deformed configurations returned to nearly cylindrical shapes (see example on Supporting Information, Figure S3). Only fully collapsed final configurations were used to parametrize the contact width formula (see eq 9).

Parameterization for Flattened Structures. The differences in contact widths between fully collapsed and flattened structures of the same outer diameter and number of walls can be approximated as a function of the heights of the flattened tubes. As shown in Supporting Information, Figure S5 and the inset of Figure S6, the heights of flattened tubes increase with diameter and then reach saturation beyond certain diameter values. The increases are linear. The deviations from linearity and subsequent saturations can be described using exponential growth functions (colored lines on Figure S6). Linear fitting of data for tubes with one to eight walls led to eqs 12−14.

We used exponential switch functions (see eq 11) to achieve smooth transitions from the linear to exponential regions. The switch points were located at the points of deviation from linearity. The values for deviation points were fit with a linear equation, which suggested the 8*N* term. Good fits for the curviness of the transition were produced using 1/*N*. This suggested the equation

$$\text{height} = (1 - H(x))D + H(x)\left(A + B\exp\left(\frac{-D}{C}\right)\right) \qquad (21)$$

for the saturation height shown in Supporting Information, Figure S6. Fitted lines are shown along with the original data points. The heights of the flattened tubes from eq 21 were used to produce equations for contact width differences (W_{corr}) between corresponding flattened and collapsed tubes. On the basis of the data, we found that the W_{corr} to height ratio was strongly dependent on *N*. This is because *N* defines the susceptibility of a tube to radial deformation and, therefore, its height. After correcting for this, we established a linear relationship by plotting 1/*N* as a function of W_{corr}/(height × N). The result was eq 10. We estimate that the error associated with the model is +3.769 nm and −0.403 nm, based on deviations of the model from the data points.

There are also other sources of uncertainty associated with the theoretical estimates for the contact widths. MM3 is considered to be among the best force fields for this type of problem. However, it is not expected to predict exact results. Also, due to computational limitations, the training sets for our fitting (see Supporting Information, Figures S3, S6, and S7) are quite far from the experimental estimates for tube sizes. Thus, although good fits were achieved, such extrapolations are always associated with uncertainty. Better estimates may be available *via* the next generation of supercomputers.

Conflict of Interest: The authors declare no competing financial interest.

Supporting Information Available: HR-TEM data relating number of CNT walls to outer diameter (Figure S1); plots of contact width *vs* diameter for collapsed (Figure S3) and flattened (Figure S7) tubes from atomistic simulations; additional plots (Figures S2 and S6) and illustrations (Figures S4 and S5) pertaining to atomistic simulations. This material is available free of charge *via* the Internet at http://pubs.acs.org.

Acknowledgment. This work was supported by ARO MURI award W911NF-09-1-0541 and NSF award CMMI-1235480. J.T.P. thanks Raul Esquivel-Sirvent for helpful discussions. The authors would like to thank Dr. Shuyou Li of the Electron Probe Instrumentation Center (EPIC) at Northwestern University for obtaining TEM images and Rodrigo Bernal for helpful discussions and assistance with digital image correlation. The authors also thank Dr. Xinqi Chen of the Keck-II Center at Northwestern University for assistance with acquiring Raman spectra of graphene-on-copper. This research used resources of the QUEST cluster at Northwestern University, WestGrid and Compute/Calcul Canada. M.R.R. gratefully acknowledges support from the Department of Defense (DoD) through the National Defense Science & Engineering Graduate Fellowship (NDSEG) Program and the Northwestern University Ryan Fellowship & International Institute for Nanotechnology. M.R.R. also thanks Rafael Soler-Crespo for helpful discussions.

REFERENCES AND NOTES

1. Zhang, M.; Atkinson, K. R.; Baughman, R. H. Multifunctional Carbon Nanotube Yarns by Downsizing an Ancient Technology. *Science* **2004**, *306*, 1358–1361.
2. Min, J.; Cai, J. Y.; Sridhar, M.; Easton, C. D.; Gengenbach, T. R.; McDonnell, J.; Humphries, W.; Lucas, S. High Performance Carbon Nanotube Spun Yarns from a Crosslinked Network. *Carbon* **2012**, *52*, 520–527.
3. Koziol, K.; Vilatela, J.; Moisala, A.; Motta, M.; Cunniff, P.; Sennett, M.; Windle, A. High-Performance Carbon Nanotube Fiber. *Science* **2007**, *318*, 1892–1895.
4. Zhang, S.; Zhu, L.; Minus, M. L.; Chae, H. G.; Jagannathan, S.; Wong, C. P.; Kowalik, J.; Roberson, L. B.; Kumar, S. Solid-State Spun Fibers and Yarns from 1-mm Long Carbon Nanotube Forests Synthesized by Water-Assisted Chemical Vapor Deposition. *J. Mater. Sci.* **2008**, *43*, 4356–4362.
5. Tran, C. D.; Humphries, W.; Smith, S. M.; Huynh, C.; Lucas, S. Improving the Tensile Strength of Carbon Nanotube Spun Yarns Using a Modified Spinning Process. *Carbon* **2009**, *47*, 2662–2670.
6. Denis-Lutard, V.; Derre, A.; Maugey, M.; Mercader, C.; Moisan, S.; Zakri, C.; Poulin, P. *New Wet Spinning Process for the Continuous Production of Polymer/Carbon Nanotubes Composite Fibers*. Recent Advances in Textile Composites: Proceedings of the 10th International Conference on Textile Composites; DEStech Publications, Inc: Lancaster, PA, 2010; pp 167−172.
7. Naraghi, M.; Filleter, T.; Moravsky, A.; Locascio, M.; Loutfy, R. O.; Espinosa, H. D. A Multiscale Study of High Performance Double-Walled Nanotube−Polymer Fibers. *ACS Nano* **2010**, *4*, 6463–6476.
8. Ryu, S.; Lee, Y.; Hwang, J. W.; Hong, S.; Kim, C.; Park, T. G.; Lee, H.; Hong, S. H. High-Strength Carbon Nanotube Fibers Fabricated by Infiltration and Curing of Mussel-Inspired Catecholamine Polymer. *Adv. Mater.* **2011**, *23*, 1971–1975.
9. Li, Y. L.; Kinloch, I. A.; Windle, A. H. Direct Spinning of Carbon Nanotube Fibers from Chemical Vapor Deposition Synthesis. *Science* **2004**, *304*, 276–278.
10. Zhang, X.; Li, Q.; Tu, Y.; Li, Y.; Coulter, J. Y.; Zheng, L.; Zhao, Y.; Jia, Q.; Peterson, D. E.; Zhu, Y. Strong Carbon-Nanotube Fibers Spun from Long Carbon-Nanotube Arrays. *Small* **2007**, *3*, 244–248.
11. Lu, W.; Zu, M.; Byun, J.-H.; Kim, B.-S.; Chou, T.-W. State of the Art of Carbon Nanotube Fibers: Opportunities and Challenges. *Adv. Mater.* **2012**, *24*, 1805–1833.
12. Peng, B.; Locascio, M.; Zapol, P.; Li, S.; Mielke, S. L.; Schatz, G. C.; Espinosa, H. D. Measurements of Near-Ultimate

Strength for Multiwalled Carbon Nanotubes and Irradiation-Induced Crosslinking Improvements. *Nat. Nanotechnol* **2008**, *3*, 626–631.
13. Locascio, M.; Peng, B.; Zapol, P.; Zhu, Y.; Li, S.; Belytschko, T.; Espinosa, H. D. Tailoring the Load Carrying Capacity of MWCNTs through Inter-Shell Atomic Bridging. *Exp. Mech.* **2009**, *49*, 169–182.
14. Yu, M.-F.; Lourie, O.; Dyer, M. J.; Moloni, K.; Kelly, T. F.; Ruoff, R. S. Strength and Breaking Mechanism of Multiwalled Carbon Nanotubes under Tensile Load. *Science* **2000**, *287*, 637–640.
15. Kis, A.; Csanyi, G.; Salvetat, J.-P.; Lee, T. N.; Couteau, E.; Kulik, A. J.; Benoit, W.; Brugger, J.; Forro, L. Reinforcement of Single-Walled Carbon Nanotube Bundles by Intertube Bridging. *Nat. Mater.* **2004**, *3*, 153–157.
16. Filleter, T.; Bernal, R.; Li, S.; Espinosa, H. D. Ultrahigh Strength and Stiffness in Cross-Linked Hierarchical Carbon Nanotube Bundles. *Adv. Mater.* **2011**, *23*, 2855–2860.
17. Banerjee, S.; Kahn, M. G. C.; Wong, S. S. Rational Chemical Strategies for Carbon Nanotube Functionalization. *Chem.—Eur. J.* **2003**, *9*, 1898–1908.
18. Banerjee, S.; Hemraj-Benny, T.; Wong, S. S. Covalent Surface Chemistry of Single-Walled Carbon Nanotubes. *Adv. Mater.* **2005**, *17*, 17–29.
19. Balasubramanian, K.; Burghard, M. Chemically Functionalized Carbon Nanotubes. *Small* **2004**, *1*, 180–192.
20. Peng, X.; Wong, S. S. Functional Covalent Chemistry of Carbon Nanotube Surfaces. *Adv. Mater.* **2009**, *21*, 625–642.
21. Tasis, D.; Tagmatarchis, N.; Bianco, A.; Prato, M. Chemistry of Carbon Nanotubes. *Chem. Rev.* **2006**, *106*, 1105–1136.
22. Gao, C.; Guo, Z.; Liu, J. H.; Huang, X. J. The New Age of Carbon Nanotubes: An Updated Review of Functionalized Carbon Nanotubes in Electrochemical Sensors. *Nanoscale* **2012**, *4*, 1948–1963.
23. Barber, A. H.; Cohen, S. R.; Eitan, A.; Schadler, L. S.; Wagner, H. D. Fracture Transitions at a Carbon-Nanotube/Polymer Interface. *Adv. Mater.* **2006**, *18*, 83–87.
24. Tsuda, T.; Ogasawara, T.; Deng, F.; Takeda, N. Direct Measurements of Interfacial Shear Strength of Multiwalled Carbon Nanotube/PEEK Composite Using a Nano-Pullout Method. *Compos. Sci. Technol.* **2011**, *71*, 1295–1300.
25. Ganesan, Y.; Peng, C.; Lu, Y.; Loya, P. E.; Moloney, P.; Barrera, E.; Yakobson, B. I.; Tour, J. M.; Ballarini, R.; Lou, J. Interface Toughness of Carbon Nanotube Reinforced Epoxy Composites. *ACS Appl. Mater. Interfaces* **2011**, *3*, 129–134.
26. Beese, A. M.; Sarkar, S.; Nair, A.; Naraghi, M.; An, Z.; Moravsky, A.; Loutfy, R. O.; Buehler, M. J.; Nguyen, S. T.; Espinosa, H. D. Bio-Inspired Carbon Nanotube−Polymer Composite Yarns with Hydrogen Bond-Mediated Lateral Interactions. *ACS Nano* **2013**, *7*, 3434–3446.
27. Naraghi, M.; Bratzel, G. H.; Filleter, T.; An, Z.; Wei, X.; Nguyen, S. T.; Buehler, M. J.; Espinosa, H. D. Atomistic Investigation of Load Transfer between DWNT Bundles "Crosslinked" by PMMA Oligomers. *Adv. Funct. Mater.* **2013**, *23*, 1883–1892.
28. Wei, X.; Naraghi, M.; Espinosa, H. D. Optimal Length Scales Emerging from Shear Load Transfer in Natural Materials: Application to Carbon-Based Nanocomposite Design. *ACS Nano* **2012**, *6*, 2333–2344.
29. Sasaki, N.; Toyoda, A.; Saitoh, H.; Itamura, N.; Ohyama, M.; Miura, K. Theoretical Simulation of Atomic-Scale Peeling of Single-Walled Carbon Nanotube from Graphite Surface. *e-J. Surf. Sci. Nanotechnol.* **2006**, *4*, 133–137.
30. Sasaki, N.; Toyoda, A.; Itamura, N.; Miura, K. Simulation of Nanoscale Peeling and Adhesion of Single-Walled Carbon Nanotube on Graphite Surface. *e-J. Surf. Sci. Nanotechnol.* **2008**, *6*, 72–78.
31. Strus, M.; Zalamea, L.; Raman, A.; Pipes, R. B.; Nguyen, C. V; Stach, E. A. Peeling Force Spectroscopy: Exposing the Adhesive Nanomechanics of One-Dimensional Nanostructures. *Nano Lett* **2008**, *8*, 544–550.
32. Strus, M. C.; Cano, C. I.; Pipes, R. B.; Nguyen, C. V.; Raman, A. Interfacial Energy between Carbon Nanotubes and Polymers Measured from Nanoscale Peel Tests in the Atomic Force Microscope. *Compos. Sci. Technol.* **2009**, *69*, 1580–1586.
33. Buchoux, J.; Bellon, L.; Marsaudon, S.; Aimé, J. P. Carbon Nanotubes Adhesion and Nanomechanical Behavior from Peeling Force Spectroscopy. *Eur. Phys. J. B* **2011**, 69–77.
34. Ishikawa, M.; Harada, R.; Sasaki, N.; Miura, K. Visualization of Nanoscale Peeling of Carbon Nanotube on Graphite. *Appl. Phys. Lett.* **2008**, *93*, 083122.
35. Ishikawa, M.; Harada, R.; Sasaki, N.; Miura, K. Adhesion and Peeling Forces of Carbon Nanotubes on a Substrate. *Phys. Rev. B* **2009**, *80*, 193406.
36. Miura, K.; Ishikawa, M.; Kitanishi, R.; Yoshimura, M.; Ueda, K.; Tatsumi, Y.; Minami, N. Bundle Structure and Sliding of Single-Walled Carbon Nanotubes Observed by Frictional-Force Microscopy. *Appl. Phys. Lett.* **2001**, *78*, 832–834.
37. Miura, K.; Takagi, T.; Kamiya, S.; Sahashi, T.; Yamauchi, M. Natural Rolling of Zigzag Multiwalled Carbon Nanotubes on Graphite. *Nano Lett.* **2001**, *1*, 161–163.
38. Ke, C.; Zheng, M.; Zhou, G.; Cui, W.; Pugno, N.; Miles, R. N. Mechanical Peeling of Free-Standing Single-Walled Carbon-Nanotube Bundles. *Small* **2010**, *6*, 438–445.
39. Sen, D.; Novoselov, K. S.; Reis, P. M.; Buehler, M. J. Tearing Graphene Sheets from Adhesive Substrates Produces Tapered Nanoribbons. *Small* **2010**, *6*, 1108–1116.
40. Ismach, A.; Druzgalski, C.; Penwell, S.; Schwartzberg, A.; Zheng, M.; Javey, A.; Bokor, J.; Zhang, Y. Direct Chemical Vapor Deposition of Graphene on Dielectric Surfaces. *Nano Lett* **2010**, *10*, 1542–1548.
41. Li, X.; Cai, W.; Colombo, L.; Ruoff, R. S. Evolution of Graphene Growth on Ni and Cu by Carbon Isotope Labeling. *Nano Lett* **2009**, *9*, 4268–4272.
42. Ferrari, A.; Meyer, J.; Scardaci, V.; Casiraghi, C.; Lazzeri, M.; Mauri, F.; Piscanec, S.; Jiang, D.; Novoselov, K. S.; Roth, S.; Geim, A. K. Raman Spectrum of Graphene and Graphene Layers. *Phys. Rev. Lett.* **2006**, *97*, 187401.
43. Kendall, K. Thin-Film Peeling-the Elastic Term. *J. Phys. D: Appl. Phys.* **1975**, *8*, 1449–1452.
44. Haskins, R. W.; Maier, R. S.; Ebeling, R. M.; Marsh, C. P.; Majure, D. L.; Bednar, A. J.; Welch, C. R.; Barker, B. C.; Wu, D. T. Tight-Binding Molecular Dynamics Study of the Role of Defects on Carbon Nanotube Moduli and Failure. *J. Chem. Phys.* **2007**, *127*, 074708.
45. Tian, J.; Cao, H.; Wu, W.; Yu, Q.; Guisinger, N. P.; Chen, Y. P. Graphene Induced Surface Reconstruction of Cu. *Nano Lett.* **2012**, *12*, 3893–3899.
46. Ponder, J. W. http://dasher.wustl.edu/tinker (accessed October 2011).
47. Sears, A.; Batra, R. C. Macroscopic Properties of Carbon Nanotubes from Molecular-Mechanics Simulations. *Phys. Rev. B* **2004**, *69*, 235406.
48. Filleter, T.; Yockel, S.; Naraghi, M.; Paci, J. T.; Compton, O. C.; Mayes, M. L.; Nguyen, S. T.; Schatz, G. C.; Espinosa, H. D. Experimental-Computational Study of Shear Interactions within Double-Walled Carbon Nanotube Bundles. *Nano Lett.* **2012**, *12*, 732–742.
49. Hertel, T.; Walkup, R. E.; Avouris, P. Deformation of Carbon Nanotubes by Surface van der Waals Forces. *Phys. Rev. B* **1998**, *58*, 13870–13873.
50. Griffith, A. A. The Phenomena of Rupture and Flow in Solids. *Philos. Trans. R. Soc., A* **1921**, *221*, 163–198.
51. Ruoff, R. S.; Tersoff, J.; Lorents, D. C.; Subramoney, S.; Chan, B. Radial Deformation of Carbon Nanotubes by van der Waals Forces. *Nature* **1993**, *364*, 514–516.
52. Park, M. H.; Jang, J. W.; Lee, C. E.; Lee, C. J. Interwall Support in Double-Walled Carbon Nanotubes Studied by Scanning Tunneling Microscopy. *Appl. Phys. Lett.* **2005**, *86*, 023110.
53. Chopra, N. G.; Benedict, L. X.; Crespi, V. H.; Cohen, M. L.; Louie, S. G.; Zettl, A. Fully Collapsed Carbon Nanotubes. *Nature* **1995**, *377*, 135–138.
54. Yu, M.-F.; Dyer, M. J.; Chen, J.; Qian, D.; Liu, W. K.; Ruoff, R. S. Locked Twist in Multiwalled Carbon-Nanotube Ribbons. *Phys. Rev. B* **2001**, *64*, 241403.
55. Zhang, S.; Khare, R.; Belytschko, T.; Hsia, K. J.; Mielke, S. L.; Schatz, G. C. Transition States and Minimum Energy Pathways for the Collapse of Carbon Nanotubes. *Phys. Rev. B* **2006**, *73*, 075423.

56. Ma, X.; Wang, H.; Yang, W. Tribological Behavior of Aligned Single-Walled Carbon Nanotubes. *J. Eng. Mater. Technol.* **2004**, *126*, 258–264.
57. Rodriguez, A. W.; Capasso, F.; Johnson, S. G. The Casimir Effect in Microstructured Geometries. *Nat. Photonics* **2011**, *5*, 211–221.
58. Kolmogorov, A. N.; Crespi, V. H. Registry-Dependent Interlayer Potential for Graphitic Systems. *Phys. Rev. B* **2005**, *71*, 235415.
59. Steele, W. A. *The Interaction of Gases with Solid Surfaces*; Pergamon Press: Oxford, UK, 1974.
60. Israelachvili, J. N. *Intermolecular and Surface Forces*; Academic Press: San Diego CA, 1992.
61. Benedict, L. X.; Chopra, N. G.; Cohen, M. L.; Zettl, A.; Louie, S. G.; Crespi, V. H. Microscopic Determination of the Interlayer Binding Energy in Graphite. *Chem. Phys. Lett.* **1998**, *286*, 490–496.
62. Zacharia, R.; Ulbricht, H.; Hertel, T. Interlayer Cohesive Energy of Graphite from Thermal Desorption of Polyaromatic Hydrocarbons. *Phys. Rev. B* **2004**, *69*, 155406.
63. Girifalco, L.; Lad, R. Energy of Cohesion, Compressibility, and the Potential Energy Functions of the Graphite System. *J. Chem. Phys.* **1956**, *25*, 693–697.
64. Parsegian, V. A. *Van Der Waals Forces: A Handbook for Biologists, Chemists, Engineers, and Physicists*; Cambridge University Press: UK, 2006.
65. Blagov, E.; Klimchitskaya, G.; Mostepanenko, V. van der Waals Interaction between a Microparticle and a Single-Walled Carbon Nanotube. *Phys. Rev. B* **2007**, *75*, 235413.
66. Koenig, S. P.; Boddeti, N. G.; Dunn, M. L.; Bunch, J. S. Ultrastrong Adhesion of Graphene Membranes. *Nat. Nanotechnol.* **2011**, *6*, 543–546.
67. Schrader, M. E.; Loeb, G. I. *Modern Approaches to Wettability: Theory and Applications*; Plenum Press: New York, 1992.
68. Schrader, M. E. Ultrahigh Vacuum Techniques in the Measurement of Contact Angles. IV. Water on Graphite (0001). *J. Phys. Chem.* **1975**, *79*, 2508–2515.
69. Schrader, M. E. Ultrahigh-Vacuum Techniques in the Measurement of Contact Angles. 5. LEED Study of the Effect of Structure on the Wettability of Graphite. *J. Phys. Chem.* **1980**, *84*, 2774–2779.
70. Bryant, P.; Gutshall, P.; Taylor, L. A Study of Mechanisms of Graphite Friction and Wear. *Wear* **1964**, *7*, 118–126.
71. Brennan, R. O. The Interlayer Binding in Graphite. *J. Chem. Phys.* **1952**, *20*, 40–48.
72. Crowell, A. D. Potential Energy Functions for Graphite. *J. Chem. Phys.* **1958**, *29*, 446–447.
73. Putnam, F. A.; Fort, T., Jr. Physical Adsorption of Patchwise Heterogeneous Surfaces. I. Heterogeneity, Two-Dimensional Phase Transitions, and Spreading Pressure of the Krypton-Graphitized Carbon Black System near 100 deg. K. *J. Phys. Chem.* **1975**, *79*, 459–467.
74. Liu, Z.; Liu, J. Z.; Cheng, Y.; Li, Z.; Wang, L.; Zheng, Q. Interlayer Binding Energy of Graphite: A Mesoscopic Determination from Deformation. *Phys. Rev. B* **2012**, *85*, 205418.
75. Mattevi, C.; Eda, G.; Agnoli, S.; Miller, S.; Mkhoyan, K. A.; Celik, O.; Mastrogiovanni, D.; Granozzi, G.; Garfunkel, E.; Chhowalla, M. Evolution of Electrical, Chemical, and Structural Properties of Transparent and Conducting Chemically Derived Graphene Thin Films. *Adv. Funct. Mater.* **2009**, *19*, 2577–2583.
76. Cai, W.; Piner, R. D.; Stadermann, F. J.; Park, S.; Shaibat, M. A.; Ishii, Y.; Yang, D.; Velamakanni, A.; An, S. J.; Stoller, M.; An, J.; Chen, D.; Ruoff, R. S. Synthesis and Solid-State NMR Structural Characterization of 13c-Labeled Graphite Oxide. *Science* **2008**, *321*, 1815–1817.
77. Obraztsov, A. N.; Obraztsova, E. A.; Tyurnina, A. V.; Zolotukhin, A. A. Chemical Vapor Deposition of Thin Graphite Films of Nanometer Thickness. *Carbon* **2007**, *45*, 2017–2021.
78. Yuzvinsky, T. D.; Fennimore, A. M.; Mickelson, W.; Esquivias, C.; Zettl, A. Precision Cutting of Nanotubes with a Low-Energy Electron Beam. *Appl. Phys. Lett.* **2005**, *86*, 053109.
79. Li, X.; Yang, W.; Liu, B. Bending Induced Rippling and Twisting of Multiwalled Carbon Nanotubes. *Phys. Rev. Lett.* **2007**, *98*, 205502.
80. Hopcroft, M. A.; Nix, W. D.; Kenny, T. W. What Is the Young's Modulus of Silicon?. *J. Microelectromech. Syst.* **2010**, *19*, 229–238.
81. Ku, H. H. Notes on the Use of Propagation of Error Formulas. *Precision Measurement and Calibration, NBS SP 300* **1969**, *1*, 331–341.
82. Humphrey, W.; Dalke, A.; Schulten, K. VMD—Visual Molecular Dynamics. *J. Mol. Graph.* **1996**, *14*, 33–38.